RESIDUAL FLUID BLOBS AND CONTACT ANGLE MEASUREMENTS FROM X-RAY IMAGES OF FLUID DISPLACEMENT

MAŠA PRODANOVIĆ[1], W. BRENT LINDQUIST[2] AND RANDALL S. SERIGHT[3]

[1]Institute for Computational Engineering and Sciences, University of Texas at Austin, 1 University Station, C0200 Austin, Texas 78712
[2]Department of Applied Mathematics and Statistics, Stony Brook University, Stony Brook, NY 11794-3600
[3]New Mexico Petroleum Recovery Research Center, New Mexico Institute of Mining and Technology, 801 Leroy Place, Socorro, NM 87801, USA

Abstract

Over the past decade a growing number of high resolution, three-dimensional, X-ray computed tomography images of multiphase porous media systems have become available, as have the number of algorithms to analyze both the pore space and the fluid partitioning imaged within the voids. Here we consider the measurement of fluid-fluid and fluid-solid surfaces at residual fluid conditions in a Berea sandstone sample. 3D reconstructions of the residual fluid blobs show qualitative behaviour which is in agreeement with conventional wisdom. We consider the measurement of fluid-solid contact angle via such images. We elucidate the challenge in identifying triple points (points with three phases in contact) and describe an algorithm for contact angle measurement. Results from application of the contact angle algorithm indicate the ability to distinguish wetting and non-wetting fluid blobs and reveal satisfactory agreement with experimental wettability measurements.

1. Introduction

Accurate geometrical information on fluid-fluid and fluid-solid interaction at the pore scale is crucial in understanding fluid displacement. In recent years, X-ray computed tomography (CT) technology [Flannery et al., 1987] has been extended to the ability to contrast fluids in the pore space of core samples [Seright et al., 2002, 2003; Turner et al., 2004; Wildenschild et al., 2002, 2005; Al-Raoush and Willson, 2005; Prodanovic et al., in press], and therefore to the study of fluid partitioning in the 3D pore space. 3D studies can help illuminate the fluid competition mechanisms at the pore level. The measurements obtained from such studies contribute naturally to network flow model computation, an important tool for predicting flow at the core scale.

In extensive studies of Berea sandstone fluid displacement experiments [Prodanovic et al., in press; Seright et al., in press], we presented results on oil and water partitioning in the pore space at residual fluid conditions, as well as the effects on residual fluid distribution due to the injection and gelation of a water-based gel. Here we analyze the residual fluid blobs from that Berea experiment. We focus on a representative subvolume

of the imaged core and categorize volumetric and surface features of all residual fluid blobs located in the subvolume. While a few residual fluid blobs studies have been reported in the literature for sphere packs, either from X-ray tomography [Culligan et al., 2004; Al-Raoush and Willson, 2005] or from solidified residual phase [Chatzis et al., 1983], to our knowledge ours is the first systematic study of residual fluid blobs in a naturally occurring, consolidated porous medium.

We focus our attention on the ability to measure contact angles from CT images. We present a robust algorithm for contact angle determination based on fluid surfaces reconstruction from segmented images and apply it to the Berea sample. The algorithm represents the addition of a valuable tool to complement existing wettability measurements.

Before discussing effects, specific to our image based procedure, that affect the accuracy of contact angle measurement, we note that there are three physical effects which lead to the expectation that a range of contact angles will be observed when making measurements from fluid displacement in core samples.

1. As time required for collecting a CT image is much longer than flow time-scales, CT imaging must occur at static flow conditions, e.g. residual conditions. Although the core may be imaged at residual drainage conditions, in the static image there is no knowledge whether, during the approach to residual conditions, a specific (part of) a fluid surface was in fact locally advancing or receding. Thus contact angle hysteresis would predict more than one contact angle.

2. Contact angles are defined from a force-balance equation (Young's equation) applied at a fluid-fluid-grain triple contact. Experimental measurements of contact angle have a length-scale component of "irreproducibility" due to surface roughness [Morrow, 1975]. Measurement of contact angle size can vary if two separate length scales (e.g. mm vs. μm) are applied to measure angles at a given triple-point.

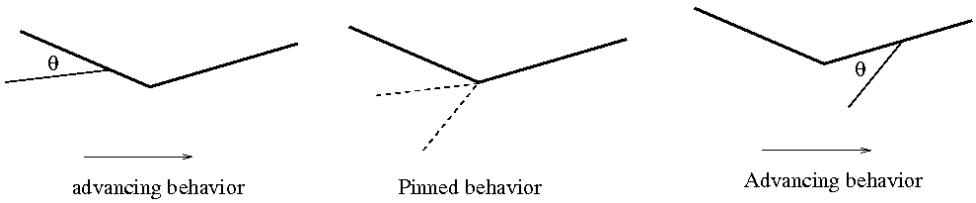

FIGURE 1. A wetting fluid blob traversing a corner in a non-flat solid surface. The interface arrives at the left side of the corner with the contact angle θ (left); the contact angle increases during a pinning period under which the meniscus swings but the triple point remains fixed (center); the interface leaves the corner when the angle reaches the value θ with respect to the right side (right).

3. Difficulties with surface regularity dependence have lead to standards for experimental measurement of contact angles; specifically to employing highly polished, planar, solid surfaces. (The contact angles associated with the two fluids involved will therefore sum to 180 degrees.) This will not be the case with grain surfaces contacted in real porous media. As shown on Fig. 1. and discussed in detail by Lindquist [in press], the contact angle

experiences a range of values during a period of "pinning" when a fluid-fluid meniscus swings around a corner of the solid surface.

2. Experimental Procedure

The image sequence analyzed here has been studied previously. For continuity, we briefly review the experimental procedure from which the images were produced; we refer the interested reader to Prodanovic et al. [in press] for greater detail.

A 6.5 mm diameter, 35 mm length core was taken from a larger Berea sample having bulk absolute permeability 0.464 μm^2 (0.47 Darcy) and porosity 22%. Experimentally determined Amott-Harvey wettability indexes taken on similar Berea cores have values ranging from 0.5 to 0.8, with an average value of 0.7. The core was saturated with brine containing 1% NaCl and 0.1% $CaCl_2$ and imaged at the tomographic facility on the X2B beam line [Deckman et al., 1991] at the National Synchrotron Light Source at Brookhaven National Laboratory. Beam energy was 33.3 keV. A 2.52 mm long section centrally located along the length of the cylindrical core was imaged at a voxel resolution of 4.93 μm. Using the experimental setup described by Seright et al. [2003], the core was then successively imaged at residual fluid conditions occurring during a sequence of floods. The experimental apparatus enabled the sequence of fluid injections to be performed without removing the core from the mounting stage. After each image, the rock core was rotated back to its initial position allowing for one-to-one voxel correspondence between the initial and subsequent images.

The fluid injection sequence was: 35 pore volumes (PV) of oil; 70 PV of brine; 10 PV of aqueous gelant; 20 PV of oil; 2.5 PV of brine. Fluid was injected with a pressure drop of 117.2 kPa across the length of the core. After gel injection, but before imaging, the core was heated to ~ 60°C for 12 hours to effect gelation. The aqueous gelant was Cr(III)-acetate-HPAM (hydrolyzed polyacrylamide) consisting of (by weight) 0.5% Alcoflood 935 HPAM, 0.0417% Cr(III) acetate, 1% NaCl, and 0.1% $CaCl_2$. The oil was hexadecane doped with 10% (by weight) iodohexadecane. The addition of iodohexadecane to the hexadecane improves the X-ray attenuation contrast between the oil and water phases (at the cost of severely reducing contrast between the oil and solid phases). All experiments were performed at room temperature except during gelation. The fluid viscosities were: brine - 10^{-3} mPa-s (1 cP), hexadecane - $3.3 \cdot 10^{-3}$ mPa-s, gelant - $20 \cdot 10^{-3}$ mPa-s.

For purposes of reference, the sequence of images will be identified as s_w (brine saturated core), s_{wr} (residual brine after oil flood), s_{or} (residual oil after brine flood), gel (post gel placement), $gels_{wr}$ (residual brine from oil flood post gel placement), and $gels_{or}$ (residual oil from brine flood post gel placement).

We note that the driving pressure gradient was reduced to zero before each residual fluid-condition image was acquired. Thus there is the expectation of local relaxation of the meniscus, which may, in fact, tend to reduce contact angle variation due to pinning.

3. Image Analysis

Our geometrical analysis of the CT images is based upon improvements and extensions to the 3DMA-Rock software package [Lindquist, 1999]. The algorithms utilized to analyze

fluid partitioning include fluid/grain and fluid/fluid segmentation, fluid-fluid and fluid-solid interface reconstruction, and the statistical description of the fluid partitioning at the scale of individual pores.

3.1. **Segmentation.** For segmentation, we employ an indicator kriging algorithm [Oh and Lindquist, 1999] which produces a voxelized interface (i.e. an interface that is the union of voxel faces) between two phases. By design, the kriging algorithm is a bi-phase segmentation algorithm; it segments phase P from its complement P^c. Thus segmentation of n phases can be achieved in $n-1$ applications of the segmentation algorithm.

The three phase (solid, oil and brine) segmentations needed were achieved as follows. The core was initally saturated with a wetting fluid (brine) and imaged. Subsequent images contained both oil and water phase in the pore space. The segmentation of the solid phase is performed on this first (two phase) brine saturated image; the solid phase location in subsequent images in the flooding sequence is inherited from its location in the first. In the subsequent images, the indicator kriging algorithm is applied only to the pore (non-solid) space to perform the segmentation of the occupying two fluid phases.

Segmentation produces false-positive and false-negative errors, which are somewhat easier to correct in solid-void segmentation than in fluid-fluid segmentation. In solid-void phase segmentation, false positives appear as isolated clusters of (apparent) grain phase voxels. Detached grains are clearly unphysical and may be due to misidentified void voxels (false positives) or because a narrow connecting grain "bridge" is below voxel resolution and the voxels comprising the bridge are identified as void (false negatives). We handle detached grains by converting them to void phase. Similarly, isolated clusters of pore space voxels are produced either by misidentified grains (false negatives) or because narrow connecting void tubes at sub-voxel resolution are lost. While isolated pores are physical, they cannot contribute to fluid motion; for all practical purposes they can be converted to grain phase. In practice, such conversions change the overall porosity by a minor fraction of a percent.

In segmenting fluids, these arguments do not apply. However, while segmentation may produce significant numbers of isolated blobs of either fluid phase, in practice such blobs occupy a negligible fraction of total pore space. We therefore choose to retain all fluid phase blobs. In our analysis, however, we impose a minimum fluid blob size requirement to protect our results from segmentation errors and finite resolution effects.

In computing connectivity of either fluid phase, it is important to choose and retain a 6-connected, 26-connected distinction between the two phases. We treat the wetting phase (brine) as 26-connected and the non-wetting phase as 6-connected. The identification of each individual **blob** of a fluid phase is achieved via grassfire algorithm (of the appropriate connectivity). Interior blobs are those not connected to the volume boundary. We compute the number, location and size of the individual blob of each fluid phase.

3.2. **Interphase surfaces generation in three phase images.** Voxelized surfaces are well known to be poor reconstructions of true surfaces; triangulated surfaces produce superior reconstructions. A triangulated interface between two phases in a volumetric image is most commonly determined by the marching cubes algorithm [Lorensen and Cline , 1987]. The key idea of the marching cubes algorithm is as follows: if two neighboring (in a 6-connected sense) voxels belong to two different phases, the interphase interface must

intersect the straight line joining the respective voxel centers. This point of intersection is identified as a vertex of the interphase surface. In a voxelized image, these surface vertices can be connected in a consistent triangulation proceeding cube-by-cube, where each cube consists of 8 neighboring voxel centers (hence the "marching cubes" designation). In a grey-scale image, the surface vertices can be chosen to follow any particular intensity contour; in a segmented (binary) image, the surface vertices are normally chosen to follow the 0.5 contour (i.e. the vertex is always at the midpoint between two voxel centers).

The application of marching cubes to locate interphase surfaces in porous media was introduced by Dalla et al. [2002]. The authors verified the algorithm on digitized representations of analytically known solid surfaces (sphere packs). The work identifies two sources of error, (1) sphere digitization effects and (2) systematic surface vertex positioning errors (i.e. systematic use of the midpoint between two voxel centers to position a surface vertex). Increasing the resolution of the digitization (decreasing voxel size) reduces the first type of errors; however, the second error cannot be similarly eliminated. For the surface area of a single sphere, the relative error due to the second source is never smaller than 8.4%.

As we deal with images at a fixed voxel resolution, both sources of error come in to play, and can be especially large for estimating surfaces of blobs comprised of small numbers of voxels.

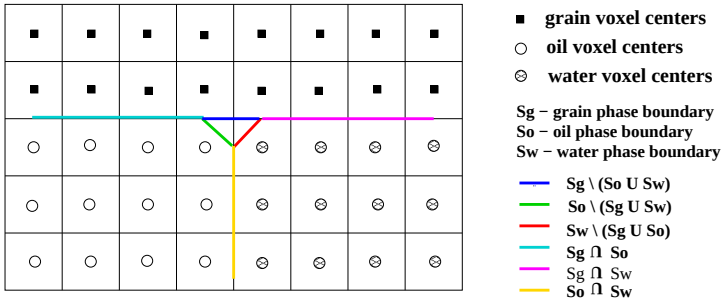

FIGURE 2. A 2D example of the surface separating three phases as determined by the marching cubes algorithm. The grain phase boundary, S_g, is the union of the cyan, blue, and magenta lines; the oil phase boundary, S_o, is the union of the cyan, green, and yellow lines; the water phase boundary, S_w, is the union of the yellow, red, and magenta lines. The triangular region bounded by the red, green and blue line segments is "exterior" to all three phases and represents the digitized version of a triple-contact line (point).

We note that the marching cubes algorithm is a two-phase surface finding algorithm; it locates the surface between phase P and P^c. Consider an image consisting of a grain phase (G) and two fluid phases, oil (O) and brine (W). Let S_g denote the interphase surface between G and G^c as determined by marching cubes. Surfaces S_o and S_w are defined analogously. Fig. 2. illustrates (in 2D) the problem with finding three-phase contact lines when employing marching cubes; the three surfaces do not meet along a line of three-phase contact. Rather the surfaces isolate a finite volume of unclassified phase. The presence of this unclassified phase region complicates estimation of fluid-grain contact angles since the oil-water interface, $S_o \cap S_w$, (yellow line in Fig. 2.) does not extend to

the grain phase boundary. Fig. 3. provides a three dimensional view of this problem for a single oil blob.

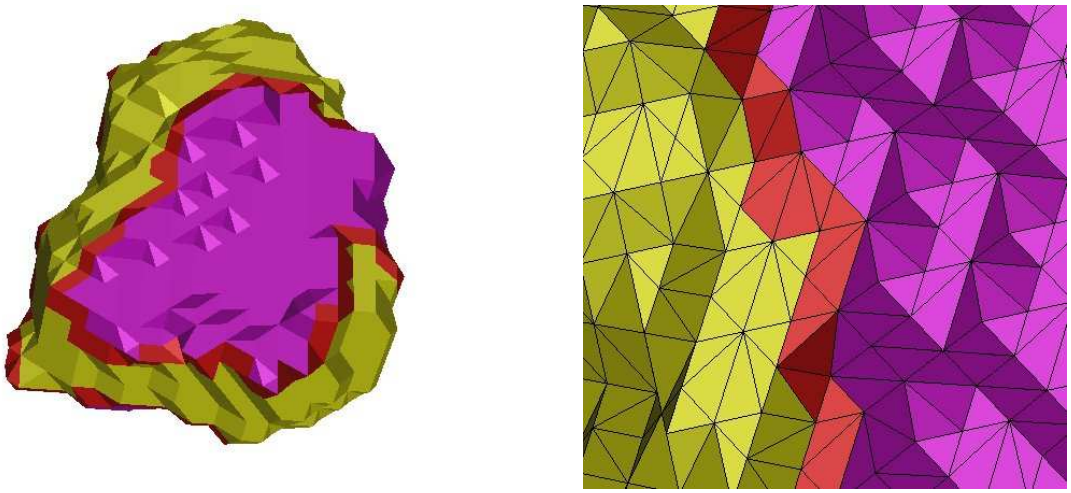

a) b)

FIGURE 3. a) View of a single oil blob extracted from the image s_{WI}. Colors correspond to the legend in Fig. 2.: magenta - the area of the blob surface in contact with grain; yellow - the area in contact with water; red - the ribbon of triangles in contact with a region of indeterminate phase. b) A magnified view of a portion of the surface, with surface triangle edges outlined for clarity. The red strip of triangles separates the oil-water surface from the oil-grain surface, preventing a direct measurement of oil-grain contact angle.

4. A CONTACT ANGLE ALGORITHM

We describe an algorithm that approximates the fluid-fluid-solid contact angles by extending the triangulated surface S_{ow} to S_g.

For notational compactness we denote surface intersection as $S_{AB} := S_A \cap S_B$. and surface exclusion by $\bar{S}_A := S_A \backslash (S_B \cup S_C)$ for any three distinct phases $A, B, C \in \{o, w, g\}$. Triangulated surfaces consist of vertices, edges and triangles. Two vertices are considered adjacent if they are joined by an edge; two triangles are considered adjacent if they share an edge. We assume consistently oriented surfaces; when surface S_A is produced by the marching cubes algorithm, its triangles are consistently oriented with the normals of all triangles pointing outwards from phase A. The marching cubes algorithm guarantees that, where the two surfaces S_A and S_B intersect, the triangle vertices of the two surfaces align perfectly but the adjacency structure of the vertices (i.e. their organization into triangles) may differ. The triangle normal directions will also be opposite for the two surfaces. Thus we take the triangles and their normals on the surface intersection S_{AB} to be inherited from S_A, and the triangles and their normals on S_{BA} to be inherited from S_B.

We have implemented the following algorithm using the triangulated surface library GTS (available at http://gts.sourceforge.net/index.html/).

Contact Angle Algorithm for an Oil-Water Surface

(1) Traverse the set V consisting of all vertices v on the intersection curve $\bar{S}_o \cap S_{ow}$ (e.g. the curve of intersection of the red and yellow surfaces in Fig. 3. b)).
(2) For each v:
   (a) Find T_{ow}, the set of all triangles from S_{ow} adjacent to v. Let $\vec{n}_{ow}$ be the average of all triangle normals in T_{ow}.
   (b) Find the set W_v of all vertices w on the intersection curve $\bar{S}_o \cap S_{og}$ that are adjacent to v.
   (c) Let T_{og} be the set of all triangles from S_{og} that are adjacent to any vertex in W_v. Let $\vec{n}_{og}$ be the average of all triangle normals in T_{og}.
   (d) Compute $\theta_o = \angle(\vec{n}_{ow}, -\vec{n}_{og})$.
(3) Analogously, find θ_w for each vertex v' on the intersection of surfaces $\bar{S}_w$ and S_{wo}. This set V' of vertices is, for the most part, the same as V.
(4) Each vertex in $V \cap V'$ has a computed value for both θ_o and θ_w. Scale the two angles as follows:

$$\theta_{os} = \frac{\theta_o}{(\theta_o + \theta_w)} \cdot 180, \qquad \theta_{ws} = \frac{\theta_w}{(\theta_o + \theta_w)} \cdot 180.$$

(5) Let $\bar{\theta}_o$ denote the value of θ_{os} averaged over all vertices in $V \cap V'$. Compute $\bar{\theta}_w$ analogously.

We consider $\bar{\theta}_o$ and $\bar{\theta}_w$ to be measures of the oil-solid and water-solid contact angles for the fluid blob in question. The scaling in step (4) attempts to correct for the measured contact angles for the non-planarity of the surface, as discussed in §1.

While the algorithm is stated for an oil-water surface, it can be obviously generalized for any two fluids.

4.1. **Algorithm validation.** There are a number of factors which combine to potentially limit the ability to determine contact angles from CT images. These include truncation effects due to finite voxel size, segmentation error (void/grain and fluid/fluid), and limitations of the marching cubes surface construction noted above. The contact angle algorithm presented above directly addresses the lack of triple-contact lines in the (union of the) marching cubes surfaces. There is however also the concern noted by Dalla et al. [2002] of a systematic error due to the fact that marching cubes places surface vertices only at midpoints between two voxels. This will limit the range of triangle orientation with respect to the coordinate axes (and therefore limit the measureable range of contact angles).

We have validated the contact angle detection algorithm with the following test.

Validation Test

Let Z denote the integers. Then $(i, j, k) \in Z^3$ denotes a voxel location in a digited space where unit distance is given by voxel length.

(1) Consider the digitized sphere S, radius r ($r \in Z$) centered at $C = (x_c, y_c, z_c) \in Z^3$ which approximates the continuum sphere

$$f(x, y, z) := (x - x_c)^2 + (y - y_c)^2 + (z - z_c)^2 - r^2 = 0 \ .$$

(2) Consider the plane P through C given by

$$h(x,y,z) := a(x-x_c)+b(y-y_c)+c(z-z_c)=0\ .$$

Identify sets of grain (G), oil (F_o) and water (F_w) voxels by

$$\begin{aligned} G &= \{(i,j,k) : h(i,j,k) \le 0\}, \\ F_o &= \{(i,j,k) : h(i,j,k) > 0 \text{ and } \ f(i,j,k) \le 0\}, \\ F_w &= \{(i,j,k) : h(i,j,k) > 0 \text{ and } \ f(i,j,k) > 0\}. \end{aligned}$$

The set F_o of oil voxels forms a digitized hemispherical blob.

(3) Translate P along its normal direction (a,b,c) in discrete units of distance. Under each successive translation, the set F_o becomes a smaller digitized sphere "cap", disappearing when P is translated r units. At each discrete position, the contact angles for the fluid phases F_o and F_w are determined using the contact angle algorithm in §4.

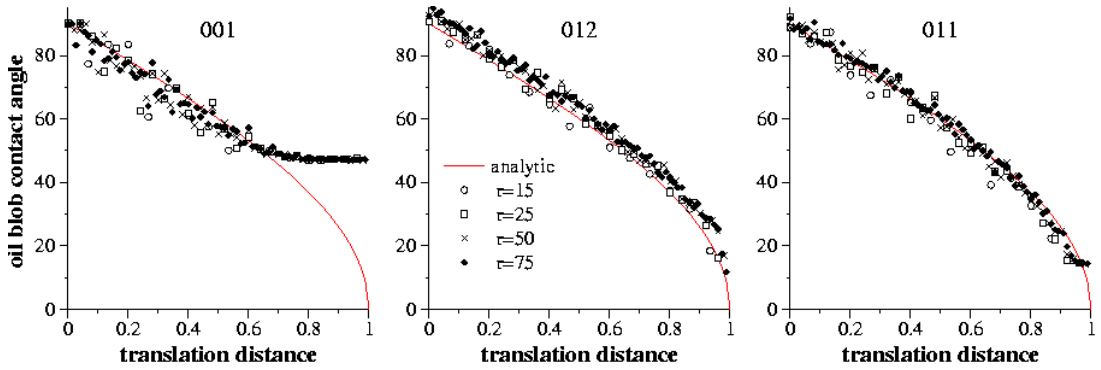

FIGURE 4. Measured contact angle $\bar{\theta}_o$ for the F_o "blob" as a function of translation distance for the plane P (translation distance is normalized relative to r) for three orientations (abc) of P.

Fig. 4. summarizes computed results for the blob contact angle $\bar{\theta}_o$ for three choices of plane orientation. If P is aligned with the coordinate axes (left plot), the smallest measurable angle for $\bar{\theta}_o$ is approx. 45 degrees (regardless of the resolution, i.e. the radius of the sphere). If P is not aligned with the grid (remaining plots) all measured angles are roughly within 10 degrees of the analytic one. In CT images of fluid blobs in geologic media, the random shapes and orientation of the pore spaces imply that the second two plots are more typical occurrences.

5. Results

To minimize against segmentation-induced misidentification errors, we consider only interior blobs of volume 10^3 voxels (0.00012 mm^3) or larger. The blobs were isolated from a 256^3 voxel subregion of a larger Berea image. Table 1. summarizes information on the blobs isolated in each image of the sequence. While the minimum volume threshold is somewhat arbitrary, choice was guided by the desire to minimize segmentation errors (as elaborated in §3.1) as well as to visualize blobs and categorize their behavior.

TABLE 1. Overall fluid saturations obtained from image analysis and the number of interior residual blobs with minimum size 1000 voxels.

			number of blobs		largest blob volume (10^{-3} mm^3)	
	s_w	s_o	water	oil	water	oil
s_{wr}	20%		28		2.97	
s_{or}		16%		58		1.22
gel		43%		45		9.71
$gels_{wr}$	29%		33		1.42	
$gels_{or}$		55%		21		1.70

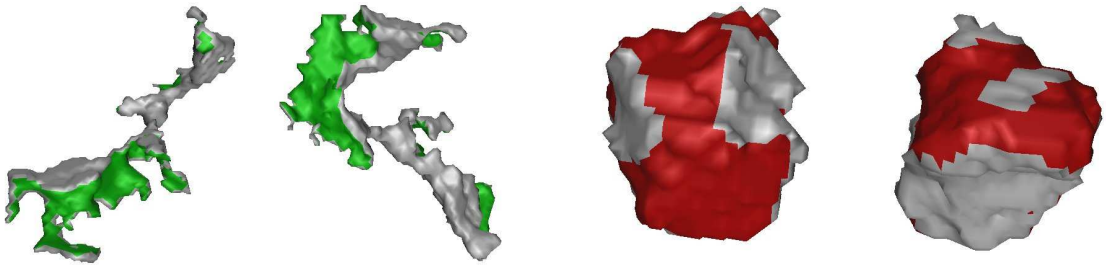

a) b)

FIGURE 5. a) Two views of a typical water blob at water residual conditions s_{wr}. The blob volume is $1.95 \cdot 10^{-4}$ mm^3. The water-grain contact surface is colored in gray; and water-oil mensicus is green. b) A typical oil blob extracted at oil residual conditions s_{or}. The blob volume is $2.57 \cdot 10^{-4}$ mm^3. The oil-grain contact surface is gray; the oil-water meniscus is red.

Using 3D graphics, visual examination of individually identified fluid blobs[1] reveals the following generalizations. A typical water blob (Fig. 5. a)) occupies at least one throat region, and its surface is topologically cylindrical. The water blob surface consists of water-grain contact and a water-oil meniscus. A large area of the water-oil meniscus tends to "follow" the water-grain surface closely (film-like behaviour). A typical oil blob (Fig. 5. b)), on the other hand, occupies a significant fraction of a pore, and the blob surface is rarely a topological cylinder.

These qualitative differences are quantified by the measurements shown in Fig. 6. Values of surface area to volume ratios (for all blobs of sufficient size) are presented in Fig. 6. a). The data show that residual water blobs have consistently larger surface area to volume ratio (230.52 mm^{-1} on average) than do residual oil blobs (129.88 mm^{-1} on average). The fraction of the blob surface in contact with grain (Fig. 6. b)) is higher for residual water blobs (water blobs' average 0.62, oil blobs' average 0.49). Fig. 6. c) plots the ratio

[1]A gallery of the fluid blob images is available at http://www.ices.utexas.edu/∼masha/blobs/main.html

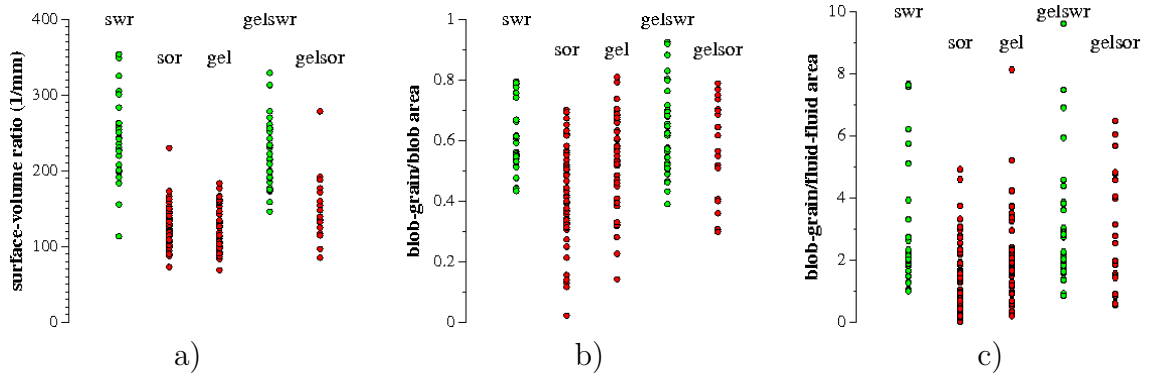

FIGURE 6. a) Surface area to volume ratio for blobs from the Berea experiment. Measurements from residual water blobs are marked green, from residual oil blobs are red. b) Blob-grain contact area (normalized to total blob surface area) for the same blobs. c) Values of the ratio of oil-water meniscus area to blob-grain area.

of grain contact to fluid-fluid meniscus area for the blobs. For residual water blobs, the average ratio is 4.49; more than twice that of the residual oil blob ratio of 2.0.

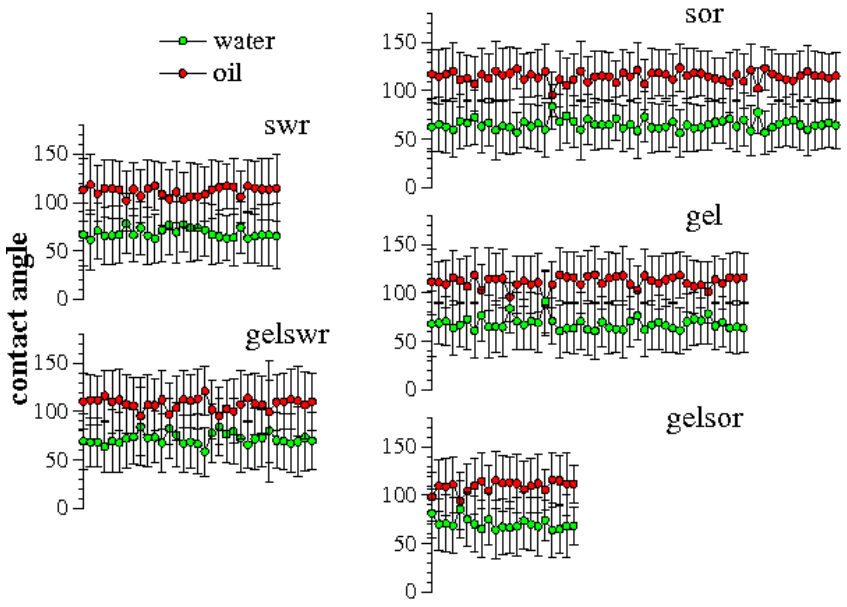

FIGURE 7. Measured oil, $\bar{\theta}_o$ (red), and water, $\bar{\theta}_w$ (green), contact angles for each residual blob identified at each residual flow condition. For each blob, we plot the mean and standard deviation of the water and oil angle along the surface contact with the solid.

The contact angle algorithm was applied to the surfaces of this set of blobs. Values of contact angle determined for each blob at each residual fluid condition are summarized in Fig. 7. For each image, the mean values (over all blobs) of the measured water-grain

TABLE 2. Measured mean contact angles (in degrees).

Image	s_{wr}	s_{or}	gel	$gels_{wr}$	$gels_{or}$
water-grain	68 ± 30	65 ± 26	68 ± 27	71 ± 30	71 ± 29
oil-grain	112 ± 30	115 ± 26	112 ± 27	109 ± 30	109 ± 29

and oil-grain contact angles are shown in Table 2. Water (wetting) and oil (non-wetting) contact angles are well distinguished. Due to rather large standard deviations we cannot state any shift in the contact angles before and after gel. We note that changing the connectivity of fluids (i.e., assuming water phase to be 6-connected and oil phase to be 26-connected) affects somewhat the number and sizes of fluid blobs, however the measured contact angle averages and standard deviations remain stable under such a change.

6. Discussion

We have shown that X-ray tomography, with voxel resolution of 5 microns, can be used to reconstruct fluid-fluid-grain interfaces in images from core samples. Visual examination of the images shows that the isolated blobs of residual fluid phase identified in these images are positioned in the pore space according to conventional wisdom. We have demonstrated an algorithm to extract measures of contact angle from such images, and shown that results obtained are sufficient to differentiate between wetting and non-wetting phases.

References

Al-Raoush, R. I., and C. S. Willson (2005), A pore-scale investigation of a multiphase porous media system, *J. Contam. Hydrol.*, 77, 67–89.

Chatzis, I., N. R. Morrow, and H. T. Lim (1983), Magnitude and detailed structure of residual oil saturation, *Soc. Petroleum. Engin. J.*, 23, 311–326.

Culligan, K. C., D. Wildenschild, B. S. B. Christensen, W. G. Gray, M. L. Rivers, and A. F. B. Tompson (2004), Interfacial area measurements for unsaturated flow through a porous medium, *Water Resour. Res.*, 40, W12413.

Dalla, E., M. Hilpert, and C. T. Miller (2002), Computation of the interfacial area for multi-fluid porous medium systems, *J. Contam. Hydrol.*, 56, 25–48.

Deckman, H. W., J. H. Dunsmuir, K. L. D'Amico, S. R. Ferguson, and B. P. Flannery (1991), Development of quantitative X-ray microtomography, *Matl. Res. Soc. Symp.*, 21

Flannery, B. P., H. W. Deckman, W. G. Roberge, and K. L. D'Amico (1987), Three-dimensional X-ray microtomography, *Science*, 237, 1439–1444.

Lindquist, W. B. (1999), 3DMA General Users Manual, Technical report, Department of Applied Mathematics and Statistics, State University of New York, Stony Brook, NY. The software is available at http://www.ams.sunysb.edu/∼lindquis/3dma/3dma_rock/3dma_rock.html

Lindquist, W. B. (in press), The Geometry of Primary Drainage, *J. Colloid Interface Sci.*

Lorensen, W. E., and H. E. Cline (1987), Marching cubes, a high resolution 3-D surface construction algorithm, *ACM Computer Graphics*, 21, 163–169.

Morrow, N. R. (1975), The effects of surface roughness on contact angle with special reference to petroleum recovery, *J. Can. Petrol. Technol.*, 14(4), 42–53.

Oh, W., and W. B. Lindquist (1999), Image thresholding by indicator kriging, *IEEE Trans. Pattern Anal. Mach. Intell.*, 21, 590–602.

Prodanovic, M., W. B. Lindquist, and R. S. Seright (in press), 3D image-based characterization of fluid displacement in a Berea core, *Adv. Water Resour.*

Seright, R. S., M. Prodanovic and W. B. Lindquist (in press), X-Ray Computed Microtomography Studies of Fluid Partitioning in Imbibition and Drainage Before and After Gel Placement, Disproportionate Permeability Reduction, *Soc. Petr. Eng. J.*

Seright, R. S., J. Liang, W. B. Lindquist, and J. H. Dunsmuir (2002), Characterizing disproportionate permeability reduction using synchrotron X-ray computed microtomography, *SPE Reservoir Evaluation and Engineering*, 5, 355–364.

Seright, R. S., J. Liang, W. B. Lindquist, and J. H. Dunsmuir (2003), Use of X-ray computed microtomography to understand why gels reduce permeability to water more than to oil, *J. Petroleum Sci. Eng.*, 39, 217–230.

Turner, M. L., L. Knufing, C. H. Arns, A. Sakellariou, T. J. Senden, A. P. Sheppard, R. M. Sok, A. Limaye, W. V. Pinczewski, and M. A. Knackstedt (2004), Three-dimensional imaging of multiphase flow in porous media, *Physica A*, 339, 166–172.

Wildenschild, D., J. W. Hopmans, M. L. Rivers, and A. J. R. Kent (2005), Quantitative analysis of flow processes in a sand using synchrotron-based X-ray microtomography, *Vadose Zone J.*, 4

Wildenschild, D., J. W. Hopmans, C. M. P. Vaz, M. L. Rivers, D. Rikard, and B. S.B. Christensen (2002), Using X-ray computed tomography in hydrology: systems, resolutions, and limitations, *J. Hydrology* 267, 285–297.